

## John C. Steuben<sup>1</sup>

Mem. ASME

Computational Multiphysics Systems Laboratory,  
Center of Materials Physics and Technology,  
Naval Research Laboratory,  
Washington, DC 20375  
e-mail: john.steuben@nrl.navy.mil

## John G. Michopoulos

Fellow ASME

Computational Multiphysics Systems Laboratory,  
Center of Materials Physics and Technology,  
Naval Research Laboratory,  
Washington, DC 20375  
e-mail: john.michopoulos@nrl.navy.mil

## Athanasios P. Iliopoulos

Mem. ASME

Computational Multiphysics Systems Laboratory,  
Center of Materials, Physics and Technology,  
Naval Research Laboratory,  
Washington, DC 20375  
e-mail: athanasios.iliopoulos@nrl.navy.mil

## Benjamin D. Graber

Computational Multiphysics Systems Laboratory,  
Center of Materials Physics and Technology,  
Naval Research Laboratory,  
Washington, DC 20375  
e-mail: benjamin.graber@nrl.navy.mil

## Andrew J. Birnbaum

Computational Multiphysics Systems Laboratory,  
Center of Materials Physics and Technology,  
Naval Research Laboratory,  
Washington, DC 20375  
e-mail: andrew.birnbaum@nrl.navy.mil

# Multiscale Tomographic Wave–Matter Interaction Modeling to Enable Artifact-Free Material Defect Reconstruction

*Technologies for material defect detection/metrology are often based on measuring the interactions between defects and waves. These interactions frequently create artifacts that skew the quantitative character of the relevant measurements. Since defects can have a significant impact on the functional behavior of the materials and structures they are embedded in, accurate knowledge of their geometric shape and size is necessary. Responding to this need, the present work introduces preliminary efforts toward a multiscale modeling and simulation framework for capturing the interactions of waves with materials bearing defect ensembles. It is first shown that conventional approaches such as ray tracing result in excessive geometric errors. Instead, a more robust method employing solutions to the wave equation (calculated using the Finite Element Method) is developed. Although the use of solutions to the general wave equation permits application of the method to many wave-based defect detection technologies, this work focuses exclusively on the application to X-ray computed tomography (XCT). A general parameterization of defect geometries based on superquadratic functions is also introduced, and the interactions of defects modeled in this fashion with X-rays are investigated. A synthetic two-dimensional demonstration problem is presented. It is shown that the combination of parameterization and modeling techniques allows the recovery of an accurate, artifact-free defect geometry utilizing classical inverse methods. The path forward to a more complete realization of this technology, including extensions to other wave-based technologies, three-dimensional problem domains, and data derived from physical experiments is outlined. [DOI: 10.1115/1.4049760]*

*Keywords: computational geometry, computational metrology, inverse methods for engineering applications, machine learning for engineering applications, multiscale modeling and simulation, physics-based simulations*

## Introduction

With only a few extraordinarily well-controlled exceptions, all materials contain defects [1]. Here, the term “defect” is used to describe localized regions featuring properties which vary from those of the surrounding material. Defects are commonly classified according to their morphology as voids, inclusions, cracks, etc. Such defects exist as ensembles spanning many length scales, from atomic-scale dislocations to macroscopic cracks and voids. An example of a defect created by lack of fusion in an additively manufactured part is illustrated in Fig. 1.

The presence of defects in engineered materials, components, and structures can have enormous deleterious performance ramifications [2]. As a result, an extensive variety of techniques have been developed to detect and identify defects in situ. Common approaches include ultrasonic [3–5], thermographic [6–8], shearographic [9–11], Lamb-wave [12–14], and X-ray tomographic (XCT) [15–17] methods. Similarly, a large body of work exists regarding the detection of defects in particular material classes, with some relevant

areas of focus including metals [18–22], composites [23–28], electronics [29–32], and biologically derived materials [16,33–36].

The available methods for defect detection are based on waves interacting with materials bearing defects. These waves may be of a single wavelength (“monochromatic”) or spectrally distributed (“polychromatic”). These waves interact via various mechanisms (refraction, scattering, etc.) with defects in a highly complex fashion. These interactions, combined with limitations in detector technology, create spurious, non-physical patterns or “artifacts” in the resulting scan data. The ultimate purpose of the present effort is to identify, implement, and validate a methodology for the removal of such artifacts from scan data, in order to accurately model and assess the performance impact of defects discovered in situ.

The present research is confined to the topic of XCT for the sake of practicality and conciseness. This choice was made due to the widespread application of XCT to performance-critical components and structures, particularly in the aerospace industry. However, the methods developed in the course of this research are based on a general form of the wave equation, and are readily extensible to other defect detection technologies. The remainder of this section is devoted to a description of XCT. This is followed by a motivational example, where the generation of scan artifacts in XCT data is demonstrated. It is shown that these artifacts introduce an unacceptable level of error in both the recovered defect geometry, and the resulting lifespan prediction based on that geometry and a simple cyclic fatigue model. In response to this shortcoming, a

<sup>1</sup>Corresponding author.

Contributed by ASME for publication in the JOURNAL OF COMPUTING AND INFORMATION SCIENCE IN ENGINEERING. Manuscript received September 25, 2020; final manuscript received December 15, 2020; published online May 10, 2021. Assoc. Editor: Mahesh Mani.

This material is declared a work of the U.S. Government and is not subject to copyright protection in the United States. Approved for public release; distribution is unlimited.

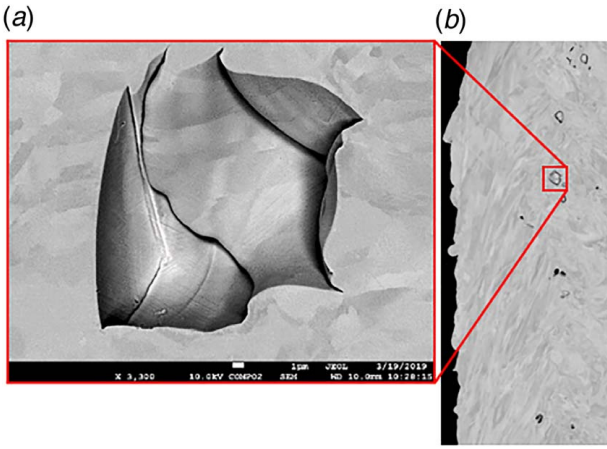


**Fig. 1** An example defect, (a) in this case a void shown in context as (b) part of a defect ensemble, imaged via electron microscopy. Note the various sizes of features associated with the single void.

new method for modeling the interactions of defects with X-rays is presented. This method is based on the use of the Finite Element Method (FEM) to calculate solutions to the Helmholtz form of the wave equation. Combined with a novel defect parameterization method, it is shown that this modeling capability enables the calculation of artifact-free defect geometry utilizing a classic inversion method. A two-dimensional synthetic experimental dataset is used to demonstrate this capability. A road-map of the many future developments necessary to mature this preliminary research in to a broadly applicable methodology concludes the paper.

A significant part of the work in the present paper was originally presented at the 2020 ASME International Design Engineering Technology/Computers and Information in Engineering conferences [37].

## X-Ray Computed Tomography

The field of tomography originates with the mathematical work of Radon [38], which was first practically applied to the area of medical imaging in the late 1960s and early 1970s. Since that time XCT has become an invaluable tool in the medical diagnostic field, and has been adopted for a wide variety of additional applications. An excellent overview of XCT as applied to the areas of engineering and materials science is given by Maire and Withers [39]. A diagram of a generic XCT process is shown in Fig. 2. A wave emitter, in this case an X-ray source, generates an interrogating wave which is directed at the test object. Rotational and/or translational actuators position the specimen relative to the interrogation waves. After passing through the test object, the transmitted wave is measured by a (2D) detector, such as a scintillator crystal or a flat-panel sensor. This process is repeated for multiple orientations of the test object, most commonly a series of small rotations about a single axis. The individual transmission X-ray scans, combined

with the pose information of the test object, are used by a reconstruction algorithm to produce an approximation of the three-dimensional object geometry.

## XCT Reconstruction Algorithms

From a computational perspective, the reconstruction algorithm is at the heart of XCT. The foundational method for XCT is the inverse radon transform, which is discussed in depth in Refs. [38,40]. While it remains the core of many XCT software tools, numerous refinements and alternatives have also been employed. Other common reconstruction algorithms include singular value decomposition [41], wavelet transforms [42], least-squares data fitting [43], and more recently, convolutional neural networks [44]. An interested reader may consult reference works such as Refs. [45,46] for a more detailed summary of available approaches.

XCT scans often exhibit noise and data artifacts [45]. For example, streaking in XCT scans is commonly observed, and is caused by combinations of undersampling (too few scans), photon starvation (inadequately energetic X-ray source), beam hardening (differential attenuation between different wavelengths of X-ray), and Compton scattering. Resultantly, many approaches have been developed to mitigate such deleterious phenomena. One common approach is filtered backprojection in the Radon transform, e.g., Refs. [47,48]. Additional approaches include those in Refs. [49,50]. The work of Jin et al. [49] is particularly relevant, as it demonstrates that incorporating even basic forward models of X-ray propagation permits scan reconstruction with greatly reduced artifacts.

There are several fundamental limitations associated with existing approaches for XCT filtering and noise-reduction limiting their applicability to the present work. The first of these limitations is due to the primarily bio-medical usage of XCT. The algorithms developed for filtering in this context typically smooth the output of the XCT data, in order to reduce visual noise and enable easier qualitative identification of scan features by human operators. Unfortunately, this process results in *removing* defect geometry information from the scan. Another issue common to existing techniques is the binarization of defect geometry into a pixel or voxel format. This step also removes important information from the scan data, particularly regarding small features. The section “Motivation” demonstrates these limitations on a simple test problem.

## Motivation

A notional example problem, demonstrating the need for improved, artifact-free defect reconstruction, is outlined in Fig. 3. A homogeneous circular domain (in 2D) is featured containing a single star-shaped defect. Synthetic tomographic data are generated by tracing rays from source points to corresponding detector points on opposing sides of the medium. The vector of detected intensities is denoted  $\mathbf{d}$ . The circular domain containing the defect is rotated about its center, and successive scans are assembled into a matrix ( $\mathbf{S}$ ) which may be visualized as a sinogram as shown in Fig. 4. This sinogram clearly shows the trace of the defect's presence.

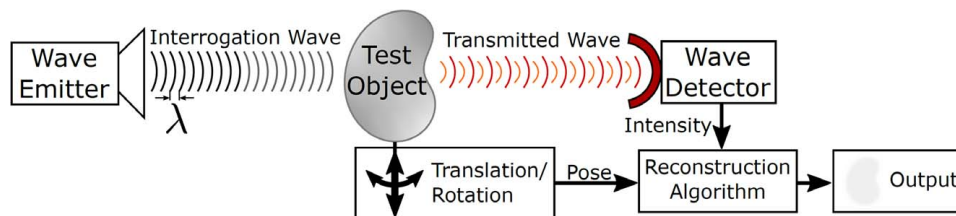


**Fig. 2** Illustration of the XCT process

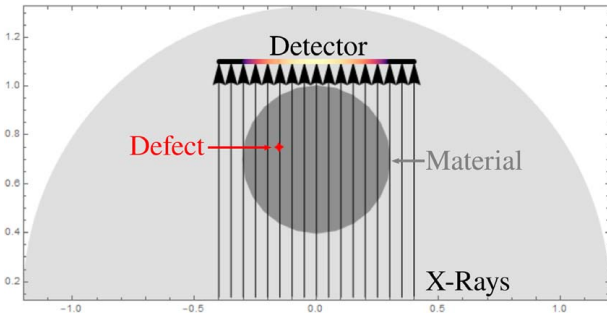


Fig. 3 Notional 2D tomography test problem. Note the linear detector array, with coloration corresponding to X-ray attenuation.

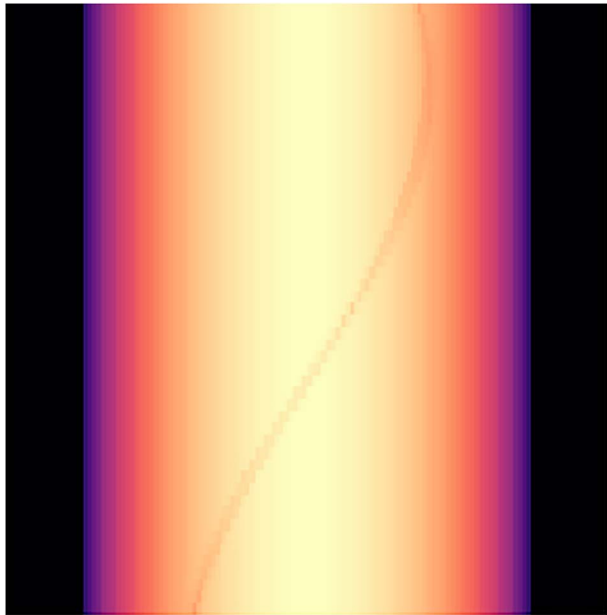


Fig. 4 Sinogram resulting from the example problem. Each row corresponds to the detector array values, for different rotations of the material domain.

The inverse radon transformation is then used to reconstruct the material/defect geometry ( $\Omega$ ):

$$\Omega = R^{-1}(\mathbf{S}) \quad (1)$$

This process is repeated utilizing several different variations, in order to generate the reconstructions shown in Fig. 5. In particular, Fig. 5 contains:

- Input material/defect geometry  $\Omega_0$ .
- A ideal reconstruction,  $\Omega = R^{-1}(R(\Omega_0))$ .
- A typical reconstruction using 100 scans (rotation of  $\pi/50$  rad, between scans) and the inverse Radon transform,  $\Omega = R^{-1}(\mathbf{S})$ .
- Same as (c) with noise reduction performed by Hann filtering and a spectral cutoff coefficient of 0.9 [51],  $\Omega = R^{-1}(f_h(\mathbf{S}, 0.9))$ .

The artifacts introduced by the reconstruction are immediately clear. The defect geometries are extracted via binarization at a 50% gray level threshold, and are shown in Fig. 6. These geometries were inserted in to a basic 2D finite-element model of a tensile test coupon in order to assess the impact of defect geometry errors on local stress/strain field intensification. The defect half-width is  $100\mu\text{m}$ , and defines a hole in a rectangular domain measuring

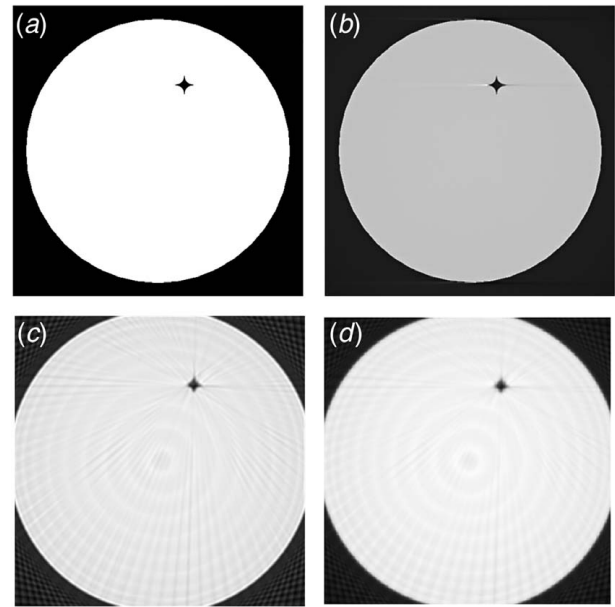


Fig. 5 Reconstructed material/defect geometry from the notional example problem. Note the shadowing, ray, and ring artifacts in (c) and (d). (a) Input, (b) ideal, (c) reconstructed, and (d) filtered.

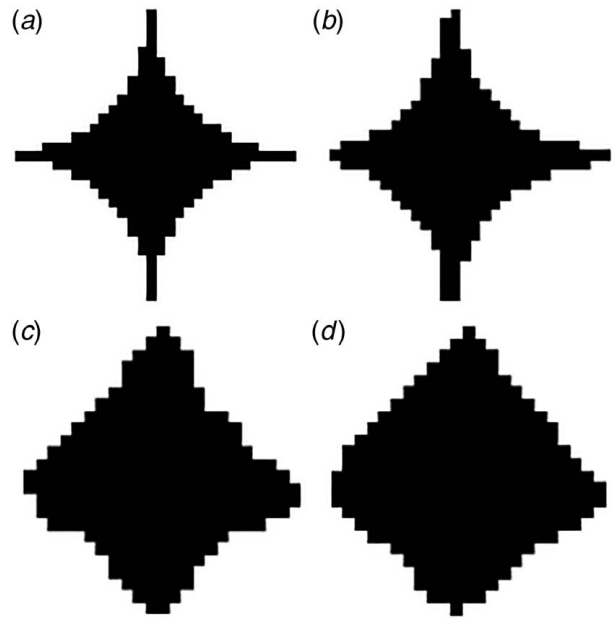
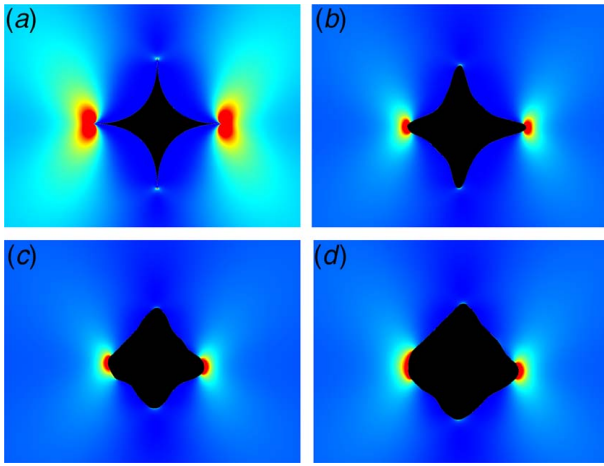


Fig. 6 Defects extracted from the notional example problem. Labels (a) through (d) correspond to those given for for Fig. 5.

$2000\mu\text{m}$  wide by  $3000\mu\text{m}$  high. The domain size was chosen to be sufficiently large to approximate an infinite elastic plane. A unit-magnitude, uniform tensile load was applied at the top edge of the domain. A plane-stress formulation was used, and the domain was discretized into approximately 500,000 second-order triangular elements. A maximum mesh size of  $0.1\mu\text{m}$  was enforced in the near-field (a circle  $150\mu\text{m}$  radius centered on the defect). The material properties of mild structural steel were used, namely,  $E = 200\text{GPa}$  and  $\nu = 0.3$ . All conditions, except defect geometry, were kept constant between the four simulations. The MUMPS solver [52] was used to solve the resulting system of equations, using default parameters. The resulting distributions of strain energy density for each geometry are shown in Fig. 7.





**Fig. 7 Intensification of strain energy density caused by the defects extracted from the notional example problem. Labels (a) through (d) correspond to those given for Fig. 5.**

**Table 1 Comparison of errors introduced by the defect reconstruction process**

Defect	Area error	Cycles to failure	Lifespan error
Input	—	1102	—
Ideal	6.1%	1560	1.42x
Reconstructed	16.8%	14,000	12.7x
Filtered	28.4%	11,360	10.3x

The finite element model was also utilized to compute the fatigue life of a domain containing each of the four defect reconstructions. A S-N criterion was applied to the von-Mises stress with a Goodman mean stress correction. The differences in predicted fatigue life are given in Table 1.

From the comparisons of Figs. 6 and 7, and the data of Table 1, it is clear that these conventional approaches to tomographic reconstruction have the potential to introduce unacceptable errors in to the lifespan prediction. The best possible case overpredicts remaining life by nearly 50%, and more realistic scenarios produce predictions with an order of magnitude error. Other research, such as Ref. [53], has found similar levels of geometric error in XCT reconstructions used for industrial metrology. The use of contouring algorithms such as Ref. [54] may reduce the binarization artifacts appreciably, but other sources of error still remain.

The poor performance of the reconstruction in this respect is unsurprising for a number of reasons. First, it is noted that the overwhelming majority of XCT research has been carried out in the biomedical context. In this context, the primary usage of XCT is diagnostic or qualitative in nature, and hence many of the derived approaches to tomograph reconstruction tend to over-smooth the underlying data in order to produce results that are easier for human interpretation. Secondly, it is seen that the underlying pixel (or in 3D, voxel) representation of defect geometry is poorly suited to some specific defect shapes. For example, the extremely sharp cusps visible in Fig. 1 require an impractically high pixel resolution to capture stress intensification properly. Finally, it is clear that the heuristic filtering and smoothing operations commonly employed may only *remove* information, as they do not encapsulate any of the relevant physics of wave-defect interaction. From these observations it follows that a physics-aware tomographic reconstruction approach, which yields parametric representation of defect geometry, may offer a great benefit in the effort to quantitatively study the effects of defects on material/structural performance.

## Methodology

Motivated by the example given in the section “Motivation”, a framework for tomographic reconstruction incorporating the physics of interactions between interrogating waves and defects is proposed. This methodology consists of three major components,

- (1) Mathematical parameterization of defects.
- (2) Forward modeling of the physical interactions of defects with interrogation waves.
- (3) Inversion of the forward model to extract defect geometry (in terms of the chosen parameterization) from experimental measurements.

The following sections describe each of these components in detail.

## Superquadratic Defects

Driven by decades of advancement in the area of computer-aided design (CAD), a wide range of generalized parametric geometry descriptions have become available. Among the most common are boundary representations (B-rep) based on Non-Uniform Rational B-Splines (NURBs) [55]. While NURBs are fully capable of representing arbitrary defects, the complexity of their implementation is prohibitive from a computational perspective. In the present work we utilize a closed-form analytic formulation based on so-called superquadratic functions,

$$\left| \frac{x - x_0}{A} \right|^r + \left| \frac{y - y_0}{B} \right|^s + \left| \frac{z - z_0}{C} \right|^t \leq 1.0 \quad (2)$$

$\{x_0, y_0, z_0\}$  defines the defect centroid,  $A, B,$  and  $C$  define the defect length along corresponding axes, and  $r, s,$  and  $t$  are shape parameters. Because  $r, s,$  and  $t$  are not constrained to integer values, this compact form may represent a wide variety of common defect shapes, as illustrated in Fig. 8. Prior work in the area of Discrete Element Methods (DEM) has also shown the utility of superquadratic functions to represent a wide variety of particle geometries [56]. For example, Figs. 8(a) and 8(b) are illustrative of defects that may form because of gaseous or rigid inclusions between layers of a composite material. Figures 8(c)–8(f) show possible inclusions in a polymer or metallic material resulting from processing contamination. Figures 8(d) and 8(g) are illustrative of cracks and delaminations that may form in layered materials. It may also be seen in Ref. [56] that an enormous variety of shapes, including cylinders, boluses, and parallelepipeds, may also be represented. The example defect of the prior section is parameterized by  $A = B = 1.0, r = s = 0.5$ . The generality of this formulation may be trivially extended by the use of arbitrary affine transformations, as well as superposition. In future work, alternative parameterizations using NURBs or volumetric fractal representations [57] will be examined as well.

## Defect Interaction Modeling

Prior work such as Ref. [49] utilizes the principles of ray optics, and ray tracing algorithms [58] to model the interaction of X-rays

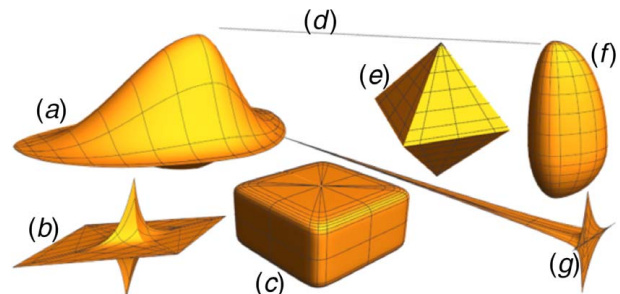


**Fig. 8 Example superquadratic defect geometries**

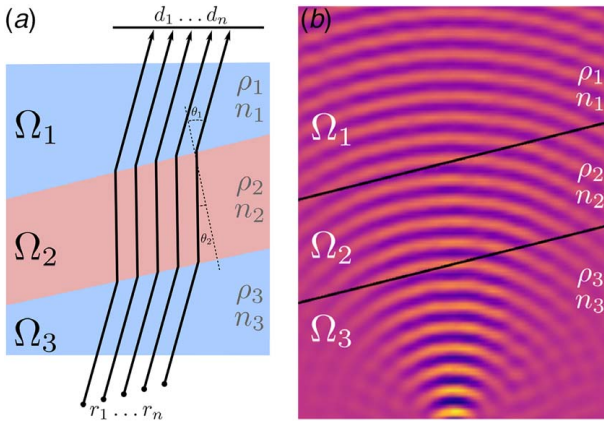


**Fig. 9 Comparison of raytracing (a) and wave-based models (b) of X-ray propagation**

with materials in XCT. While such approaches are computationally expedient, consideration of the multi-scale geometric features of defects reveals a problem: *many defects have features that are of a similar scale to the wavelength of interrogating X-rays*. Examples of such features are the sharp cusps seen in Fig. 1. This necessitates the modeling of X-rays as wave phenomena, as illustrated conceptually in Fig. 9. Instead of rays propagating through various domains ( $\Omega$ ), the X-rays are modeled using the wave equation.

The treatment used in the present work is not a comprehensive treatment of X-ray phenomena, but rather a minimal example to motivate more detailed research in the future. For analytical convenience the time-harmonic relation is expressed using the complex exponential relationship

$$p(t, x) = |p(x)|e^{i\omega t} \quad (3)$$

In particular, the present work utilizes the Helmholtz frequency-domain partial differential equation (PDE) model of the wave equation:

$$\nabla \cdot \left\{ -\frac{1}{\rho} \nabla p(x) \right\} - \frac{\omega^2}{\rho c^2} p(x) = Q_1 + Q_2 \quad (4)$$

where  $p(x)$  is amplitude at position  $x$ ,  $\rho$  is material density,  $c$  is wave speed, and

$$\omega = 2\pi \frac{c}{\lambda} \quad (5)$$

with  $\lambda$  denoting wavelength. The  $Q_1$  and  $Q_2$  terms are Neumann-type radiation boundary conditions,

$$Q_1 = \frac{i\omega}{\rho c} p(x) + r \frac{2i\omega}{\rho c}, \quad x \in \Gamma_{src} \quad (6)$$

$$Q_2 = \frac{i\omega}{\rho c} p(x), \quad x \in \Gamma_{env} \quad (7)$$

$Q_1$  corresponds to the X-ray source, driven at frequency  $r$  and is active on the  $\Gamma_1$  portion of the domain geometry.  $Q_2$  corresponds to an absorbing boundary condition on the outer boundary of the problem domain. This domain and the associated variables are illustrated in Fig. 10. It is also notable that the properties  $c$  and  $\rho$  are defined to be piecewise functions of  $x$ :

$$\rho = \begin{cases} \rho_e, & x \in \Omega_e \\ \rho_m, & x \in \Omega_m \\ \rho_d, & x \in \Omega_d \end{cases} \quad (8)$$

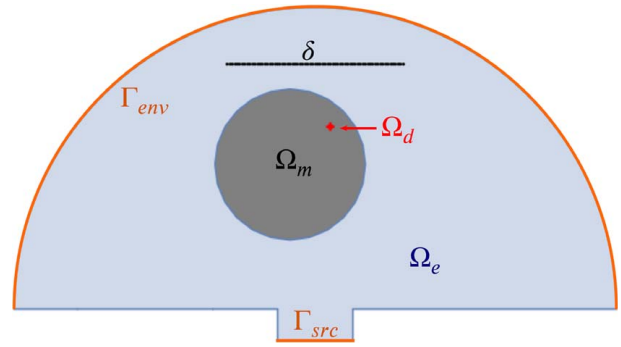


**Fig. 10 Illustration of wave simulation domains and variables**

$$c = \begin{cases} c_e, & x \in \Omega_e \\ c_m, & x \in \Omega_m \\ c_d, & x \in \Omega_d \end{cases} \quad (9)$$

where the subscripts  $e$ ,  $m$ , and  $d$  denote environment, material, and defect (respectively). The X-ray detector is represented by a series of points ( $\delta$ ) at which  $p$  may be measured.

Equation (4) is discretized and solved using the FEM. Notably, this discretization may be performed in two or three dimensions, without reformulation of the underlying equations. For simplicity and computational expediency, the present work utilizes a 2D example problem and associated discretization. The development of more general and complete FE models in 3D, incorporating additional physical phenomena such as realistic source and detector behavior, will be a major area of effort in the future.

### Inversion Method

The section “Defect Interaction Modeling” defines a “forward” model. For a given combination of material, defect, and X-ray properties, the model predicts the X-ray intensity measured by the detector. For example, Fig. 11 shows a comparison between the detected intensity for an empty X-ray chamber, the same chamber containing a defect-free material, and a defect-bearing material. The large difference between the signals from non-defective and defective materials indicates that there is significant information about the defect structure conveyed in these data.

In order to quantitatively characterize the geometry of unknown defects from experimental X-ray data, this model must be inverted. This inversion may be accomplished via any of a large number of techniques [59]. In this case, a method previously developed by

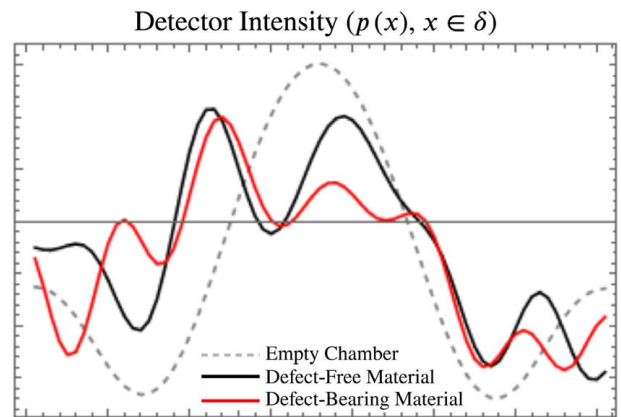


**Fig. 11 Example comparison of detector intensity for the arrangement shown in Fig. 10**

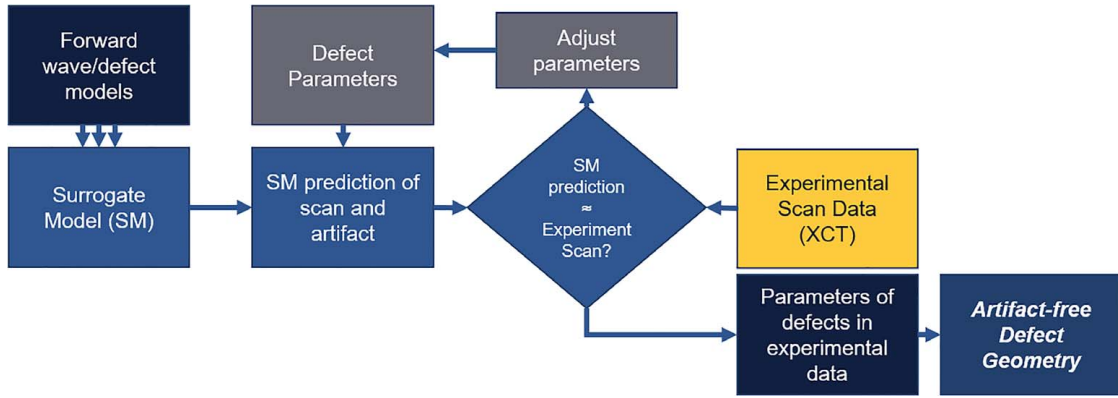


Fig. 12 Operation of the surrogate-based inversion and defect characterization algorithm

the authors for composite material characterization [60] is employed. First, the forward model is run  $i$  times, for multiple defect geometry parameter values, using a latin-hypercube sampling strategy. For each run, the detector response  $\delta_i$  is recorded. Each such dataset consists of  $n_j$  discrete observations of field intensity ( $\delta_{ij}$ ). For the 2D example problem of the present work, these sampling points are taken along a line, corresponding to a 1D detector format. For the 3D case, the sampling points would be defined on a 2D plane, corresponding to the dimensions of a flat-panel or scintillating crystal X-ray detector.

With the sampling of the forward model completed, a family of surrogate models is constructed. Each such model captures the variation of intensity at detector location  $j$  as a closed-form function of the sampled defect parameters  $\mathbf{a}$ , and is denoted  $s_j(\mathbf{a})$ . When an experimental measurement is made (denoted  $\delta_j^e$ ) it may be compared to the surrogate model. Numerical optimization techniques may be used to minimize an objective function defined as follows:

$$\mathbf{a}^e \equiv \operatorname{argminf}(\mathbf{a}) \quad (10)$$

$$f(\mathbf{a}) = \sum_{j=1}^{n_j} \left\| \delta_j^e - s_j(\mathbf{a}) \right\|_2 \quad (11)$$

$$\text{s.t. } \mathbf{a}_{i, \min} \leq \mathbf{a}_i \leq \mathbf{a}_{i, \max} \quad (12)$$

and determine the parameters of the defects present in the experimental scan ( $\mathbf{a}^e$ ). A flow diagram illustrating the operation of this optimization algorithm is shown in Fig. 12.

### Example Application

The methodology outlined in the section “Inversion Method” is generic in nature, and will require a great deal of refinement to become a practical and useful tool for defect analysis. In order to justify this effort, in this section the application of the methodology to a simple synthetic test problem is demonstrated.

The geometry illustrated in Fig. 10 was used, with a 30 mm circular material object bearing an off-center star-shaped defect. These domains were meshed using approximately 145,000 second-order triangular elements. As before, second-order triangular elements are employed. Elements within  $\Omega_d$  are constrained to have an edge length no greater than  $1 \mu\text{m}$ , those within  $\Omega_m$  (which is a circle of  $500 \mu\text{m}$  radius) are no larger than  $10 \mu\text{m}$ , and those in  $\Omega_e$  are no larger than 1000 mm. The Neumann boundary conditions of Eqs. (6) and (7) were enforced, with  $c_e = 343.4$  and  $\rho_e = 1.2$  (the values for air at standard temperature and pressure). For simplicity, the other parameters were defined  $c_m = 10c_e$ ,  $c_d = 0.5c_e$ ,  $\rho_m = 10\rho_e$ , and  $\rho_d = 0.5\rho_e$ . Any of the commonly available FEM solvers may be employed to solve the Helmholtz equation under these conditions. In the present work, the MATHEMATICA [61]

computing system is employed for discretization and solution. Although the numerical solver used by MATHEMATICA is proprietary, it gives identical results to those calculated using the aforementioned scumpms sparse/direct solver.

Solution of the FEM required 5 s on a laptop computer with a 6-core Intel Xeon processor (2.7 GHz clock frequency) and 64 Gb of system memory. These results of one run of the FEM are shown in Fig. 13. The defect parameters space were defined by  $0.5 \leq A \leq 1.5$ ,  $0.5 \leq B \leq 1.5$ ,  $0.1 \leq r \leq 0.9$ , and  $r = s$ . This three-parameter space was sampled in a uniform,  $5 \times 5 \times 5$  grid to generate samples for the surrogate model. The surrogate model was defined by the linear interpolation of these data. A synthetic experimental dataset was generated by running the FEM model a final time, at  $A = B = 1.01$ ,  $r = s = 0.013125$  (a point not in the data used to generate the surrogate).

To solve the minimization problem the Nelder–Mead optimization algorithm [62] was employed. The optimizer’s reflection ( $\alpha$ ), expansion ( $\gamma$ ), contraction ( $\beta$ ), and shrinkage ( $\rho$ ) coefficients were assigned the typical default values [63] of  $\alpha = 1$ ,  $\gamma = 2$ ,  $\beta = 0.5$ , and  $\rho = 0.5$ . The optimization used 100 randomized starting points. The final result returned was by the optimization algorithm  $A = 1.01$ ,  $B = 1.01$ ,  $r = s = 0.0131336$ . This corresponds to an error of 0.06%. This result is two orders of magnitude better than that achieved using conventional approaches, as described previously.

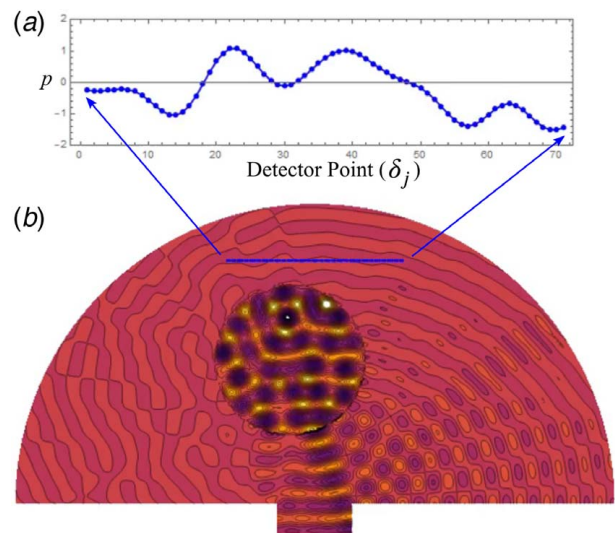


Fig. 13 Example simulation generating a sample for the surrogate model: (a) the wave magnitude  $p$  at each detector point ( $\delta_j$ ) and (b) contour plot of wave magnitude  $p$  throughout the domain, with the location of the detector points indicated



This very low error is a strong indication that the problem structure is well suited to inversion in this fashion, and suggests that further refinements of this approach are justified.

## Conclusions and Future Work

The previous sections have outlined a new method for the geometric reconstruction of defects from XCT data without the introduction of spurious artifacts. A motivational example was presented to illustrate the enormous effect that these artifacts have, resulting in especially severe over-estimation of structural fatigue life. To address this issue physics-based models, namely, solutions to the Helmholtz wave equation achieved using Finite Element methods, have been used to model the interactions of X-rays with materials bearing defects. This model utilizes a superquadratic parametric model of defect geometry. It has been shown that these techniques may be used to recover defect geometry from synthetic experimental data using a model inversion technique. The defect geometry recovered in this fashion exhibits no artifacts, and far lower error than is possible using existing methods based on ray tracing.

Although the present work has focused on XCT technology, the novel use of the general wave equation readily enables its use for other wave-based defect detection methods. Extension to such methods (i.e., ultrasonic mechanical waves) requires only the determination of the correct wave parameters (i.e.,  $c$  and  $\rho$ ) and the implementation of appropriate boundary conditions. The formulation employed by the present work is also readily applicable to three-dimensional defect reconstruction, requiring discretization and solution (but not reformulation) of the relevant wave equation in three dimensions. While the immediate work regarding the further development of this method will continue to focus on XCT, the generality required for extending to other techniques will be maintained and explored when possible.

The examples presented in this paper are extremely simple in nature, and necessarily omit many aspects of real XCT systems. In order to further develop the proposed method into a practical and useful tool, a great deal of future effort is required. Several of the most important modeling developments will include:

- (1) Enrichment of the wave model used to represent X-ray/material interactions. The modeling of various scattering phenomena will be particularly important.
- (2) Inclusion of more realistic source and detector physics including polychromatic wavelengths, and nonlinear transformations applied to the detected signal.
- (3) Extension of the model to three dimensions, with the goal of modeling cone-beam micro-tomography (uCT) systems commonly employed within the materials science context.

Further improvements to the other elements of the methodology will also be required. These may be conducted in parallel with the efforts listed previously. Important topics will include:

- (1) Identification of the best available defect geometry parameterizations. Possible approaches may include the superquadratic forms of the present work, B-rep geometry derived using NURBs or other geometry kernels, or volumetric fractal representations.
- (2) Selection of the best surrogate or reduced-order modeling approaches to employ for inversion. The linear interpolation of the present work will likely require excessively dense sampling when applied to geometries with larger numbers of parameters.
- (3) Exploration of sequential or adaptive sampling schemes for generating the data for building the surrogate models.
- (4) Selection of the best numerical optimization tools for solving the minimization problem necessary to recover the defect geometry.

In addition to these extensions and improvements, rigorous experimental validation of the methodology will be conducted.

This will be accomplished by the fabrication of test specimens containing defects of known geometry. Composite coupons, likely of the well-characterized AS4/3501-6 carbon-epoxy system, containing inclusions of polymer which are highly translucent to X-ray radiation will be manufactured. The geometry of these inclusions will be precisely measured using appropriate 3D-scanning or microscopic metrology techniques before specimen fabrication. The specimens will then be scanned using a highly accurate Zeiss Xradia 520 Versa micro-tomography system (uCT). The data gathered from these scans will be analyzed via the inversion methodology outlined in this work. Validation will be achieved by comparison of the predicted geometry to the actual defect geometry. Importantly, these predictions will be made in a “blind” fashion in order to prevent over-fitting of the surrogate models. Multiple validation experiments containing representative defect geometries will demonstrate that the methodology is sufficiently general. Additionally, after the blind comparison has been made the test articles will be measured using a destructive technique such as serial sectioning. This will provide a second independent validation that the methodology predicts defect geometry with sufficiently high accuracy. Additionally, this step will ensure that no *unintentional* defects have been introduced into the validation experiment.

Despite the magnitude of these future efforts, the proposed methodology offers unique and potentially important features. The ability to extract artifact-free, high accuracy defect geometries from XCT and uCT data will offer great utility in the lifespan estimation of components and structures. Importantly, this will not require extensive “human in the loop” scan segmentation efforts, as is required by ongoing machine-learning research. Therefore this capability may also be utilized in high-throughput experimental contexts, such as automated acceptance and qualification testing. With additional effort, the methodology may eventually become broadly applicable to many wave-based non-destructive testing technologies.

## Acknowledgment

The authors acknowledge support for this work by the Office of Naval Research through the Naval Research Laboratory’s core funding.

## Conflict of Interest

There are no conflicts of interest.

## Data Availability Statement

The datasets generated and supporting the findings of this article are obtainable from the corresponding author upon reasonable request.

## References

- [1] Macpherson, A., 2012, *Atomic Mechanics of Solids*, Elsevier Science. ISSN, Amsterdam, The Netherlands.
- [2] Murakami, Y., 2012, “Material Defects as the Basis of Fatigue Design,” *Int. J. Fatigue*, **41**, pp. 2–10. Fatigue Design & Material Defects.
- [3] Schmerr, L. W., 2016, *Fundamentals of Ultrasonic Nondestructive Evaluation*, Springer, New York.
- [4] Schmerr, L., and Song, J.-S., 2007, *Ultrasonic Nondestructive Evaluation Systems*, Springer, New York.
- [5] Zhang, J., Drinkwater, B. W., Wilcox, P. D., and Hunter, A. J., 2010, “Defect Detection Using Ultrasonic Arrays: The Multi-mode Total Focusing Method,” *NDT Int.*, **43**(2), pp. 123–133.
- [6] Maldague, X., and Marinetti, S., 1996, “Pulse Phase Infrared Thermography,” *J. Appl. Phys.*, **79**(5), pp. 2694–2698.
- [7] Maldague, X., 2000, “Applications of Infrared Thermography in Nondestructive Evaluation,” *Trends Opt. Nondestruct. Testing*, **1**(1), pp. 591–609.
- [8] Maldague, X. P., 2012, *Nondestructive Evaluation of Materials by Infrared Thermography*, Springer Science & Business Media, Berlin, Germany.
- [9] Hung, Y., 1982, “Shearography: A New Optical Method for Strain Measurement and Nondestructive Testing,” *Opt. Eng.*, **21**(3), p. 213391.

- [10] Francis, D., Tatam, R., and Groves, R., 2010, "Shearography Technology and Applications: a Review," *Meas. Sci. Technol.*, **21**(10), p. 102001.
- [11] Ruuvzek, R., Lohonka, R., and Jiron, J., 2006, "Ultrasonic C-scan and Shearography Ndi Techniques Evaluation of Impact Defects Identification," *NDT Int.*, **39**(2), pp. 132–142.
- [12] Kessler, S. S., Spearing, S. M., and Soutis, C., 2002, "Damage Detection in Composite Materials Using Lamb Wave Methods," *Smart Mater. Struct.*, **11**(2), p. 269.
- [13] Leonard, K. R., Malyarenko, E. V., and Hinders, M. K., 2002, "Ultrasonic Lamb Wave Tomography," *Inverse Prob.*, **18**(6), p. 1795.
- [14] Gibson, A., and Popovics, J. S., 2005, "Lamb Wave Basis for Impact-echo Method Analysis," *J. Eng. Mech.*, **131**(4), pp. 438–443.
- [15] Elliott, J. C., and Dover, S. D., 1982, "X-ray Microtomography," *J. Microsc.*, **126**(2), pp. 211–213.
- [16] Rueggeger, P., Koller, B., and Muller, R., 1996, "A Microtomographic System for the Nondestructive Evaluation of Bone Architecture," *Calcif. Tissue. Int.*, **58**(1), pp. 24–29.
- [17] Buffiere, J.-Y., Ferrie, E., Proudhon, H., and Ludwig, W., 2006, "Three-Dimensional Visualisation of Fatigue Cracks in Metals Using High Resolution Synchrotron X-ray Micro-tomography," *Mater. Sci. Technol.*, **22**(9), pp. 1019–1024.
- [18] Ainsworth, R., 1984, "The Assessment of Defects in Structures of Strain Hardening Material," *Eng. Fract. Mech.*, **19**(4), pp. 633–642.
- [19] Ph Papaalias, M., Roberts, C., and Davis, C., 2008, "A Review on Non-destructive Evaluation of Rails: State-of-the-art and Future Development," *Proc. Inst. Mech. Eng., Part F: J. Rail Rapid Trans.*, **222**(4), pp. 367–384.
- [20] Marrow, T., Buffiere, J.-Y., Withers, P., Johnson, G., and Engelberg, D., 2004, "High Resolution X-ray Tomography of Short Fatigue Crack Nucleation in Austempered Ductile Cast Iron," *Int. J. Fatigue*, **26**(7), pp. 717–725.
- [21] Nicoletto, G., Konečná, R., and Fintova, S., 2012, "Characterization of Microshrinkage Casting Defects of Al-si Alloys by X-ray Computed Tomography and Metallography," *Int. J. Fatigue*, **41**, pp. 39–46.
- [22] Rosado, L. S., Santos, T. G., Piedade, M., Ramos, P. M., and Vilaça, P., 2010, "Advanced Technique for Non-destructive Testing of Friction Stir Welding of Metals," *Measurement*, **43**(8), pp. 1021–1030.
- [23] Adams, R., and Cawley, P., 1988, "A Review of Defect Types and Nondestructive Testing Techniques for Composites and Bonded Joints," *NDT Int.*, **21**(4), pp. 208–222.
- [24] Gholizadeh, S., 2016, "A Review of Non-destructive Testing Methods of Composite Materials," *Proc. Struct. Int.*, **1**, pp. 50–57.
- [25] Kaiser, H., Karbhari, V., and Sikorsky, C., 2004, "Non-Destructive Testing Techniques for RP Rehabilitated Concrete. II: An Assessment," *Int. J. Mater. Product Tech.*, **21**(5), pp. 385–401.
- [26] Amenabar, I., Lopez, F., and Mendikute, A., 2013, "In Introductory Review to the Non-Destructive Testing of Composite Mater," *J. Infrared., Millimeter., Terahertz. Waves.*, **34**(2), pp. 152–169.
- [27] Milne, J., and Reynolds, W., 1985, "The Non-Destructive Evaluation of Composites and Other Materials by Thermal Pulse Video Thermography," *Thermosense VII: Thermal Infrared Sensing for Diagnostics and Control*, A. G. Kantsios, ed., Vol. 520, International Society for Optics and Photonics, Cambridge, MA, pp. 119–122.
- [28] Hung, Y., 1996, "Shearography for Non-Destructive Evaluation of Composite Structures," *Optics Lasers Eng.*, **24**(2–3), pp. 161–182.
- [29] Chen, H., Guo, F., Liu, Y., Huang, T., Zheng, B., Ananth, N., Xu, Z., Gao, W., and Gao, C., 2017, "A Defect-Free Principle for Advanced Graphene Cathode of Aluminum-ion Battery," *Adv. Mater.*, **29**(12), p. 1605958.
- [30] Fisher, C. A., Kuganathan, N., and Islam, M. S., 2013, "Defect Chemistry and Lithium-Ion Migration in Polymorphs of the Cathode Material  $\text{Li}_2\text{MnSiO}_4$ ," *J. Mater. Chem. A.*, **1**(13), pp. 4207–4214.
- [31] Kawamura, T., Sano, H., Furuta, M., Yoshioka, T., and Miyata, Y., 1994, "Defect Detection and Defect Removal Apparatus of Thin Film Electronic Device," Nov. 15. US Patent No. 5,365,034.
- [32] Moore, T. D., Vanderstraeten, D., and Forsell, P. M., 2002, "Three-Dimensional X-ray Laminography as a Tool for Detection and Characterization of Bga Package Defects," *IEEE Trans. Components Pack. Technol.*, **25**(2), pp. 224–229.
- [33] e Silva, J. M. d. S., Zanette, I., Noël, P. B., Cardoso, M. B., Kimm, M. A., and Pfeiffer, F., 2015, "Three-Dimensional Non-Destructive Soft-Tissue Visualization with X-ray Staining Micro-tomography," *Sci. Rep.*, **5**(1), pp. 1–7.
- [34] Tafforeau, P., Boistel, R., Boller, E., Bravin, A., Brunet, M., Chaimanee, Y., Cloetens, P., Feist, M., Hosszowska, J., Jaeger, J.J., Kay, R.F., Lazzari, V., Marivaux, L., Nel, A., Nemoz, C., Thibault, X., Vignaud, P., and Zabler, S., 2006, "Applications of X-ray Synchrotron Microtomography for Non-Destructive 3d Studies of Paleontological Specimens," *Appl. Phys. A.*, **83**(2), pp. 195–202.
- [35] Schatzki, T., Haff, R., Young, R., Can, I., Le, L., and Toyofuku, N., 1997, "Defect Detection in Apples by Means of X-ray Imaging," *Trans. ASAE*, **40**(5), pp. 1407–1415.
- [36] Meinlschmidt, P., 2005, "Thermographic Detection of Defects in Wood and Wood-Based Materials," 14th International Symposium of Nondestructive Testing of Wood, Honnover, Germany, May 2–4, pp. 1–6.
- [37] Steuben, J. C., Michopoulos, J. G., Iliopoulos, A. P., Graber, B. D., and Birnbaum, A. J., 2020, "Multiscale Tomographic Wave-Matter Interaction Modeling to Enable Artifact-Free Material Defect Reconstruction," ASME 2020 International Design Engineering Technical Conferences and Computers and Information in Engineering Conference, Virtual Conference, Aug. 17–19, p. V009T09A010.
- [38] Radon, J., 1986, "On the Determination of Functions From Their Integral Values Along Certain Manifolds," *IEEE Trans. Med. Imaging*, **5**(4), pp. 170–176.
- [39] Maire, E., and Withers, P. J., 2014, "Quantitative X-ray Tomography," *Int. Mater. Rev.*, **59**(1), pp. 1–43.
- [40] Durrani, T., and Bisset, D., 1984, "The Radon Transform and Its Properties," *Geophysics*, **49**(8), pp. 1180–1187.
- [41] Yuasa, T., Akiba, M., Takeda, T., Kazama, M., Hoshino, A., Watanabe, Y., Hyodo, K., Dilmanian, F. A., Akatsuka, T., and Itai, Y., 1997, "Reconstruction Method for Fluorescent X-ray Computed Tomography by Least-squares Method Using Singular Value Decomposition," *IEEE. Trans. Nucl. Sci.*, **44**(1), pp. 54–62.
- [42] Rantala, M., Vanska, S., Jarvenpaa, S., Kalke, M., Lassas, M., Moberg, J., and Siltanen, S., 2006, "Wavelet-Based Reconstruction for Limited-Angle X-ray Tomography," *IEEE Trans. Med. Imaging*, **25**(2), pp. 210–217.
- [43] Wang, J., Li, T., Lu, H., and Liang, Z., 2006, "Penalized Weighted Least-Squares Approach to Sinogram Noise Reduction and Image Reconstruction for Low-Dose X-Ray Computed Tomography," *IEEE Trans. Med. Imaging*, **25**(10), pp. 1272–1283.
- [44] Gupta, H., Jin, K. H., Nguyen, H. Q., McCann, M. T., and Unser, M., 2018, "CNN-Based Projected Gradient Descent for Consistent Ct Image Reconstruction," *IEEE Trans. Med. Imaging*, **37**(6), pp. 1440–1453.
- [45] Hsieh, J., 2003, *Computed Tomography: Principles, Design, Artifacts, and Recent Advances* (SPIE Press monograph), SPIE Press, Bellingham, WA.
- [46] Herman, G., 2009, *Fundamentals of Computerized Tomography: Image Reconstruction From Projections* (Advances in Computer Vision and Pattern Recognition), Springer, London.
- [47] Dasch, C. J., 1992, "One-Dimensional Tomography: A Comparison of Abel, Onion-Peeling, and Filtered Backprojection Methods," *Appl. Opt.*, **31**(8), pp. 1146–1152.
- [48] Katsevich, A., 2004, "An Improved Exact Filtered Backprojection Algorithm for Spiral Computed Tomography," *Adv. Appl. Math.*, **32**(4), pp. 681–697.
- [49] Jin, P., Bouman, C. A., and Sauer, K. D., 2013, "A Method for Simultaneous Image Reconstruction and Beam Hardening Correction," 2013 IEEE Nuclear Science Symposium and Medical Imaging Conference (2013 NSS/MIC), Seoul, South Korea, Oct. 27–Nov. 2, IEEE, pp. 1–5.
- [50] Boas, F. E., and Fleischmann, D., 2011, "Evaluation of Two Iterative Techniques for Reducing Metal Artifacts in Computed Tomography," *Radiology*, **259**(3), pp. 894–902.
- [51] Lyra, M., and Ploussi, A., 2011, "Filtering in Spect Image Reconstruction," *Int. J. Biomed. Imaging*, **2011**, p. 693795.
- [52] Amestoy, P., Buttari, A., L'Excellent, J.-Y., and Mary, T., 2019, "Performance and Scalability of the Block Low-Rank Multifrontal Factorization on Multicore Architectures," *ACM Trans. Math. Software*, **45**, pp. 2:1–2:26.
- [53] Xue, L., Suzuki, H., Ohtake, Y., Fujimoto, H., Abe, M., Sato, O., and Takatsuji, T., 2015, "Numerical Analysis of the Feldkamp–Davis–Kress Effect on Industrial X-Ray Computed Tomography for Dimensional Metrology," *ASME J. Comput. Inf. Sci. Eng.*, **15**(2), p. 021008.
- [54] Shammaa, H., Suzuki, H., and Ohtake, Y., 2011, "Creeping Contours: A Multilabel Image Segmentation Method for Extracting Boundary Surfaces of Parts in Volumetric Images," *ASME J. Comput. Inf. Sci. Eng.*, **11**(1), p. 011007.
- [55] de Boor, C., 2001, *A Practical Guide to Splines* (Applied Mathematical Sciences), Springer, New York.
- [56] Podlozhnyuk, A., Pirker, S., and Kloss, C., 2017, "Efficient Implementation of Superquadric Particles in Discrete Element Method Within An Open-source Framework," *Comput. Particle Mech.*, **4**(1), pp. 101–118.
- [57] Michopoulos, J. G., and Iliopoulos, A., 2013, "Complete High Dimensional Inverse Characterization of Fractal Surfaces and Volumes," *ASME J. Comput. Inf. Sci. Eng.*, **13**(1), p. 011001.
- [58] Levoy, M., 1990, "Efficient Ray Tracing of Volume Data," *ACM Trans. Graphics (TOG)*, **9**(3), pp. 245–261.
- [59] Schweiger, M., and Arridge, S. R., 2014, "The Toast++ Software Suite for Forward and Inverse Modeling in Optical Tomography," *J. Biomed. Opt.*, **19**(4), p. 040801.
- [60] Steuben, J., Michopoulos, J., Iliopoulos, A., and Turner, C., 2015, "Inverse Characterization of Composite Materials Via Surrogate Modeling," *Composite Struct.*, **132**, pp. 694–708.
- [61] Inc., W. R. Mathematica, Version 11.3. Champaign, IL, 2018.
- [62] Luersen, M. A., and Le Riche, R., 2004, "Globalized Nelder–Mead Method for Engineering Optimization," *Comput. Struct.*, **82**(23–26), pp. 2251–2260.
- [63] Lagarias, J. C., Reeds, J. A., Wright, M. H., and Wright, P. E., 1998, "Convergence Properties of the Nelder–Mead Simplex Method in Low Dimensions," *SIAM J. Optim.*, **9**(1), pp. 112–147.